# Aqueous PVP-to-HOC Conversion Enables Binder/Current-Collector Free Flexible LMO Cathodes with High Energy

Uyanga Nyamaa[a1], Oyunbayar Nyamaa[a1], Jeong-Hyeon Yang[b], Yon-Mo Sung[a], Jung-pil Noh[a] *

[a]Department of Smart Energy and Mechanical Engineering, Gyeongsang National University, Tongyeong-haeanro 2, Tongyeong 53064, Korea

[b]Department of Mechanical System Engineering, Gyeongsang National University, Tongyeong-haeanro 2, Tongyeong 53064, Korea

[1] Contribute equally to this work

* Corresponding author

*Corresponding author Email: nohjp@gnu.ac.kr

## Contents

## 1. Characteristics and Electrochemical results of composite cathodes

**Table S1.** Comparison of untreated vs. thermally treated PVP on CNT/LMO at 300 °C under inert atmosphere.

| Feature | Untreated PVP | Treated PVP |
|---|---|---|
| State | Polymeric, $sp^3$-hybridized | Partially carbonized, $sp^2$ domains begin forming |
| Electrical conductivity | Insulating | Improved (due to early $sp^2$ formation) |
| Surface interaction | Strong via polar groups (C=O, N) | Still strong, with possibly better chemical anchoring due to reactive intermediates |
| Electrolyte wettability | High (hydrophilic PVP) | Retained, with added benefit of more stable surface chemistry |
| Structural support | Acts as a dispersant | Acts as a semi-conductive matrix and transitional carbon layer |
| Mechanical flexibility | Flexible organic polymer | More rigid, but beginning to act like a carbon buffer shell |
| Thermal/chemical stability | Poor | Improved (more resistant to electrolyte attack or cycling degradation) |
| Function in electrode design | Aids dispersion and uniform mixing | Begins to improve conductivity and electron pathways |

Figure S1 displays the XRD patterns of the PVP surfactant before and after heat treatment at 300°C in an argon atmosphere. The XRD pattern of the as-received PVP shows a broad and diffuse halo, characteristic of its amorphous structure. After thermal treatment, the pattern still reflects largely amorphous characteristics, but the emergence of small, sharp diffraction peaks suggests the formation of minor crystalline domains [1]. These features indicate partial structural rearrangement or carbonization of PVP during via controlled conversion, which may contribute to the formation of a thin hybrid organic-carbon matrix in the electrode.

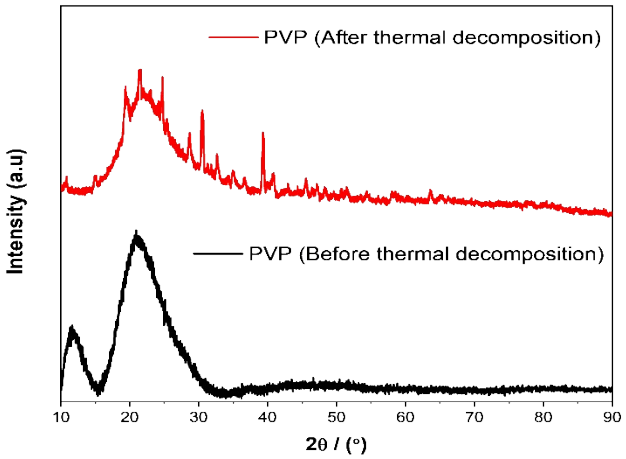


Figure S1. XRD patterns of polyvinylpyrrolidone (PVP) before and after via controlled conversion at 300 °C under argon. The as-received PVP shows an amorphous halo, while heat-treated PVP remains largely amorphous with the emergence of minor crystalline domains, indicating partial structural rearrangement and carbonization.

For fair comparison of conductivity, all CNT/LMO composite films and reference LMO/Al electrodes were fabricated with a consistent thickness of ~250 μm. This ensured that conductivity differences originated from interfacial structure rather than electrode geometry. The intrinsic conductivity of conventional binders and surfactants is orders of magnitude lower than that of carbon nanotube frameworks. Reported values are summarized in Table S1 [2-5]. These values highlight the insulating nature of PVDF and PVP compared with CNTs [6], reinforcing that the via controlled conversion of PVP into a partially graphitized carbon residue is essential for creating a conductive hybrid matrix in HOC-CNT/LMO electrodes.

**Table S2.** Electrical conductivity values of common binders/surfactants (PVDF, PVP), highlighting the insulating nature of polymers relative to CNT networks.

| Polymer name | Dielectric constant | Electrical conductivity | Type | Main structure |
|---|---|---|---|---|
| PVDF | ~6-12 | ~$10^{-11}$ S $cm^{-1}$ | Semi-crystalline fluoropolymer | Electronegative $–CF_2$ groups |
| PVP | ~3.5-6 | ~$10^{-9}$ S $cm^{-1}$ | Amorphous, water-soluble | Polar, less electronegative groups |

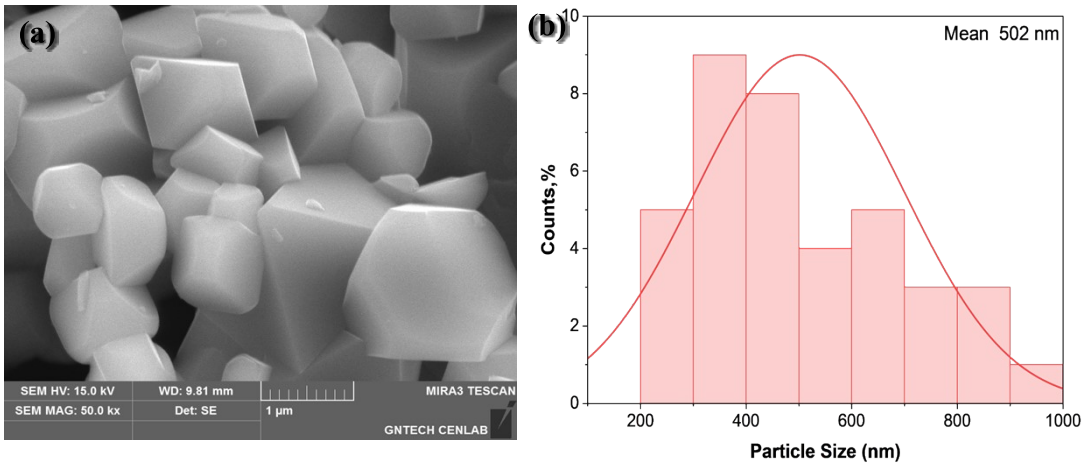


Figure S2. FE-SEM surface images of (a) LMO particle (scale bar in: 1μm), and (d) particle-size distribution.

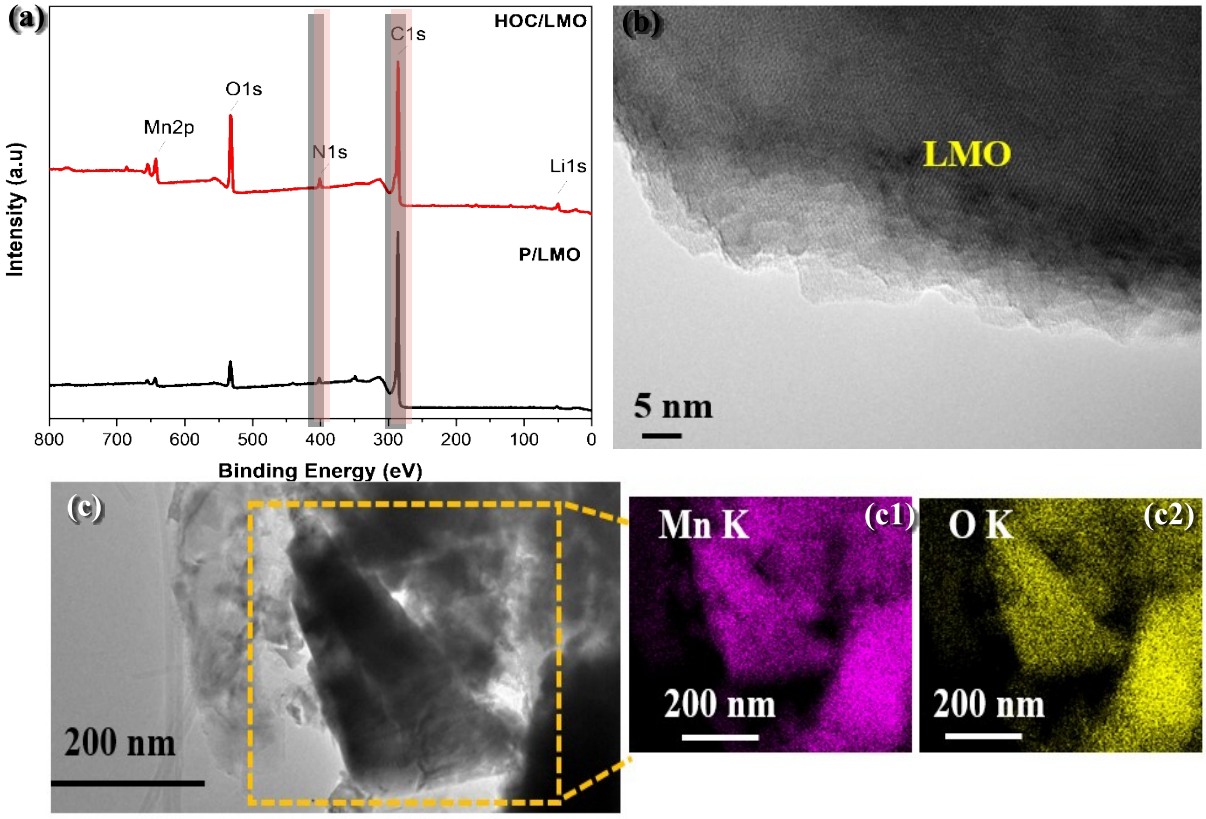


Figure S3. XPS survey spectra of (a) LMO particles, and HR-TEM images of (b) uncoated LMO (scale bar: 5 nm). EDS elemental mapping of (c-c2) pristine LMO showing the spatial distribution

of Mn, O, C, and N (scale bar: 200 nm).

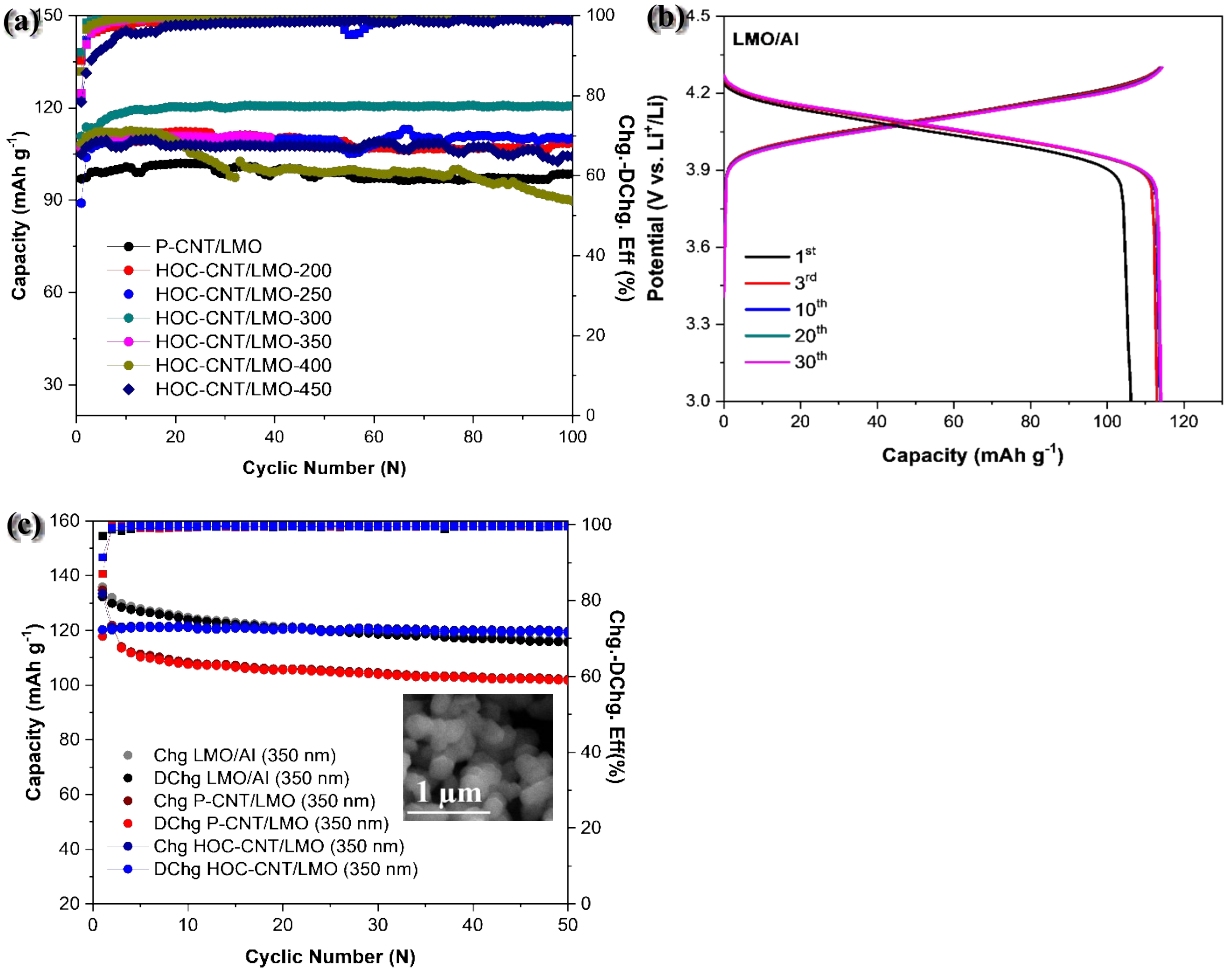


Figure S4. Charge/discharge cycling performance of (a) P-CNT/LMO electrodes subjected to via controlled conversion at different temperatures, and charge/discharge capacity profiles of (b) LMO/AI cathode at cut-off voltages of 4.3- 3.0 V under a 0.5C rate. Cycling performance of (c) pristine LMO/Al, P-CNT/LMO, and HOC-CNT/LMO electrodes using submicron $LiMn_2O_4$ (~350 nm), measured at 4.3-3.0 V under a 0.5C rate (inset: FE-SEM image of LMO particles).

**Table S3.** Electrochemical performance of CNT/LMO cathodes treated at different via controlled conversion temperatures.

| Sample | 1st Charge/ Discharge capacity (mAh $g^{-1}$) | Initial CE (%) | Charge/ Discharge capacity after 100 cycles (mAh $g^{-1}$) | Capacity retention (%) |
|---|---|---|---|---|
| P-CNT/LMO | 110/96.9 | 88 | 99.8/98.6 | 99.9 |
| HOC-CNT/LMO-200 | 121.4/107.0 | 89 | 108.5/108.4 | 99.9 |
| HOC-CNT/LMO-250 | 112.6/89.0 | 79 | 100.1/100.1 | 99.9 |
| HOC-CNT/LMO-300 | 121.2/111.0 | 92 | 121.0/120.8 | 99.9 |
| HOC-CNT/LMO-350 | 132.3/107.2 | 81 | 99.8/99.77 | 93.3 |
| HOC-CNT/LMO-400 | 126.0/108.4 | 86 | 89.9/89.84 | 83.0 |
| HOC-CNT/LMO-450 | 126.3/105.0 | 79 | 104.35/104.3 | 99.3 |

ESP maps visualize the surface polarity experienced by a test charge [7]. Broad green/yellow plateaus indicate weakly polarized, delocalized regions (favorable for close π–π contact), while red pockets mark localized electron-rich sites (e.g., carbonyls, heteroatom lone pairs). HOC displays an extended near neutral π surface with only shallow red features at N/O/edge sites, pointing to a smooth electrostatic landscape and coherent contact with $sp^2$ scaffolds. PVP exhibits deep, localized red basins centered on lactam carbonyls and a discontinuous low-polarity surface, consistent with strong local binding but limited extended stacking. As these are gas-phase fragments, interpretations are qualitative and intended to contextualize the experimental conductivity and $R_{ct}$ trends.

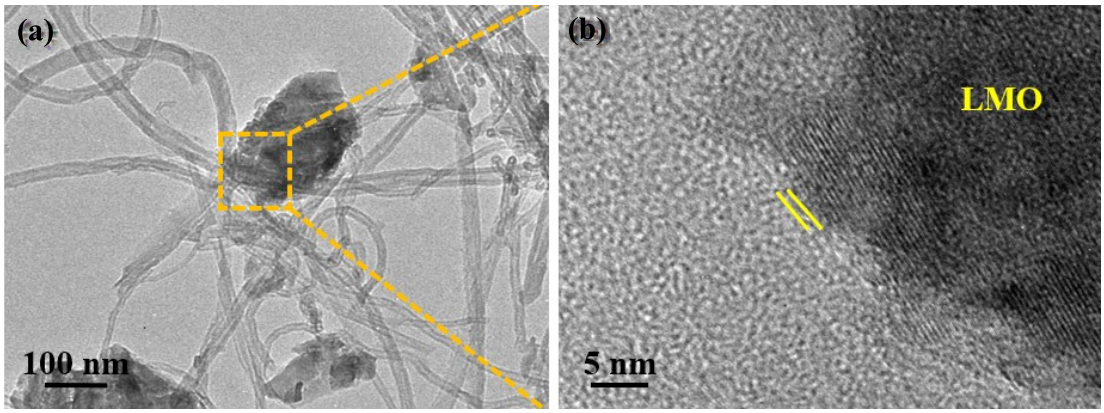


Figure S5. Post-cycling HR-TEM image of the HOC-CNT/LMO cathode after 100 cycles. The preserved lattice fringes observed at the LMO interface (scale bar: (a) 100 nm and (b) 5 nm) indicate maintained crystallinity and interfacial stability, confirming the protective effect of the hybrid organic-carbon (HOC) layer against structural degradation and parasitic surface reactions during cycling.

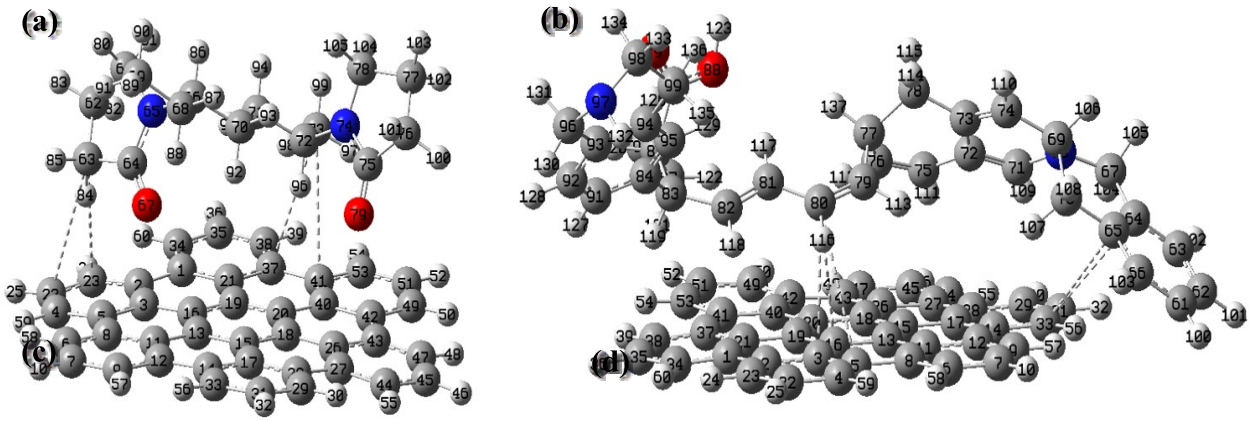

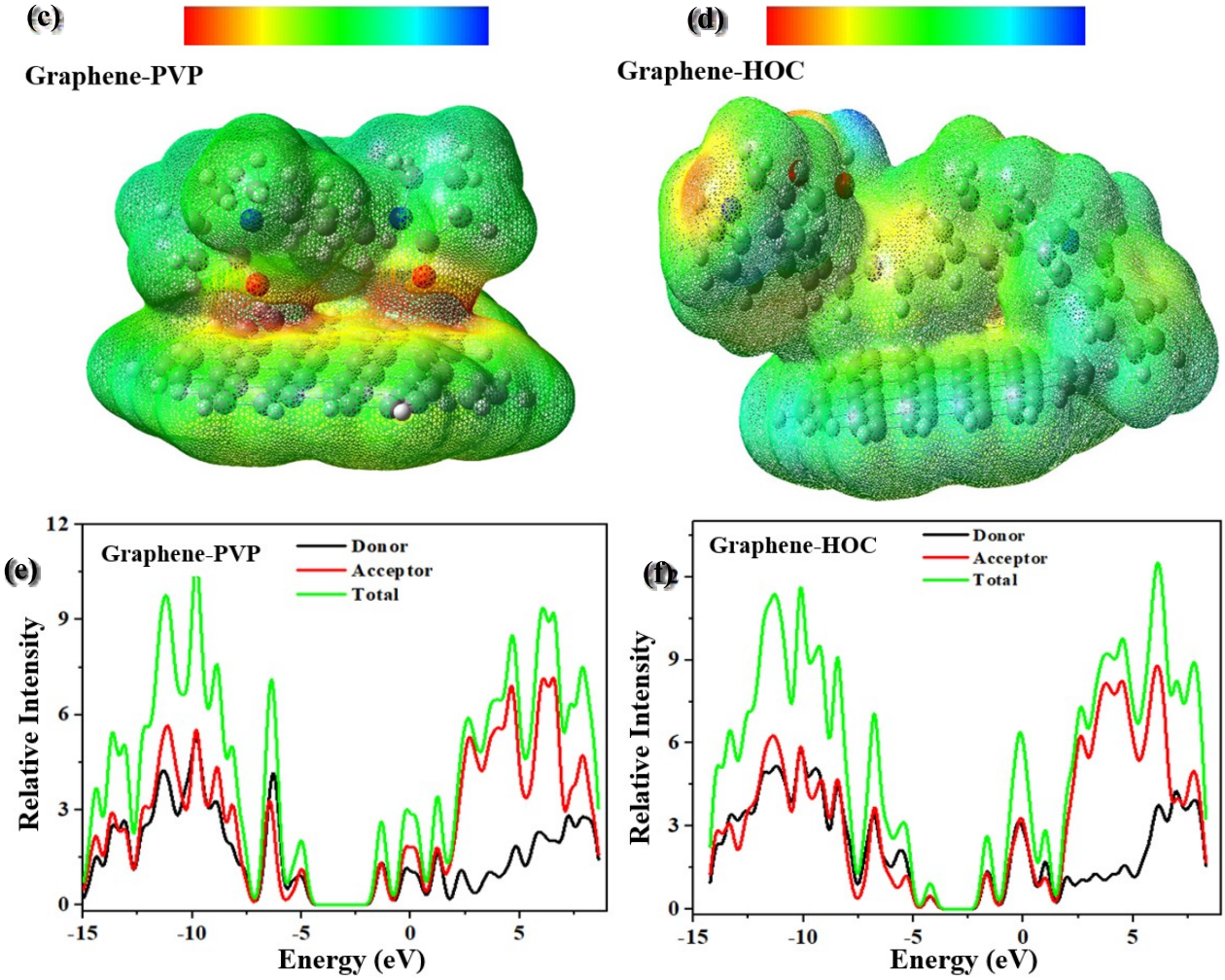


Figure S6. Qualitative interfacial electronic descriptors of graphene-polymer-derived models (PVP and HOC). DFT-optimized graphene-PVP and graphene-HOC model structures and electrostatic potential (ESP) mapped on the electron-density isosurfaces for (a, c) graphene-PVP and (b, d) graphene-HOC systems, calculated at the B3LYP/6-31G(d,p) level in the gas phase. These results provide qualitative insight into charge distribution and polarization trends at the graphene-polymer contact, complementing the interfacial electronic coupling analysis discussed in the main text. Color scale in atomic units: red = negative, green ≈ neutral, blue = positive. DOS of (e) graphene-PVP and (f) graphene-HOC interfacial models.

## 2. Electrochemical results of full cell

The bending performance of the HOC-CNT/LMO@PC-CNT/LTO full cell was systematically evaluated under repeated bending cycles with a bending radius of 8 mm. Figure S6 (d) show cycling performance of HOC-CNT/LMO@PC-CNT/LTO full cells under bending, after 5,000 bending cycles, and after 10,000 bending cycles. The results demonstrate negligible capacity loss and high Coulombic efficiency, confirming excellent mechanical resilience.

**Table S4.** Charge/discharge capacities and capacity retention of HOC-CNT/LMO@PC-CNT/LTO full cells under bending.

| Condition | Cycle number (N) | Charge/ Discharge capacity (mAh $g^{-1}$) | CE (%) | Capacity retention (%) |
|---|---|---|---|---|
| Unbent (baseline) | 25 | 71.0/70.5 | 99.3 | 99.0 ($1^{st}$→$25^{th}$) |
| After 5,000 bends | 25 | 69.3/68.7 | 99.1 | 98.8 ($26^{th}$→$51^{st}$) |
| After 10,000 bends | 29 | 66.0/65.3 | 99.0 | 98.0 ($51^{st}$→$80^{th}$) |

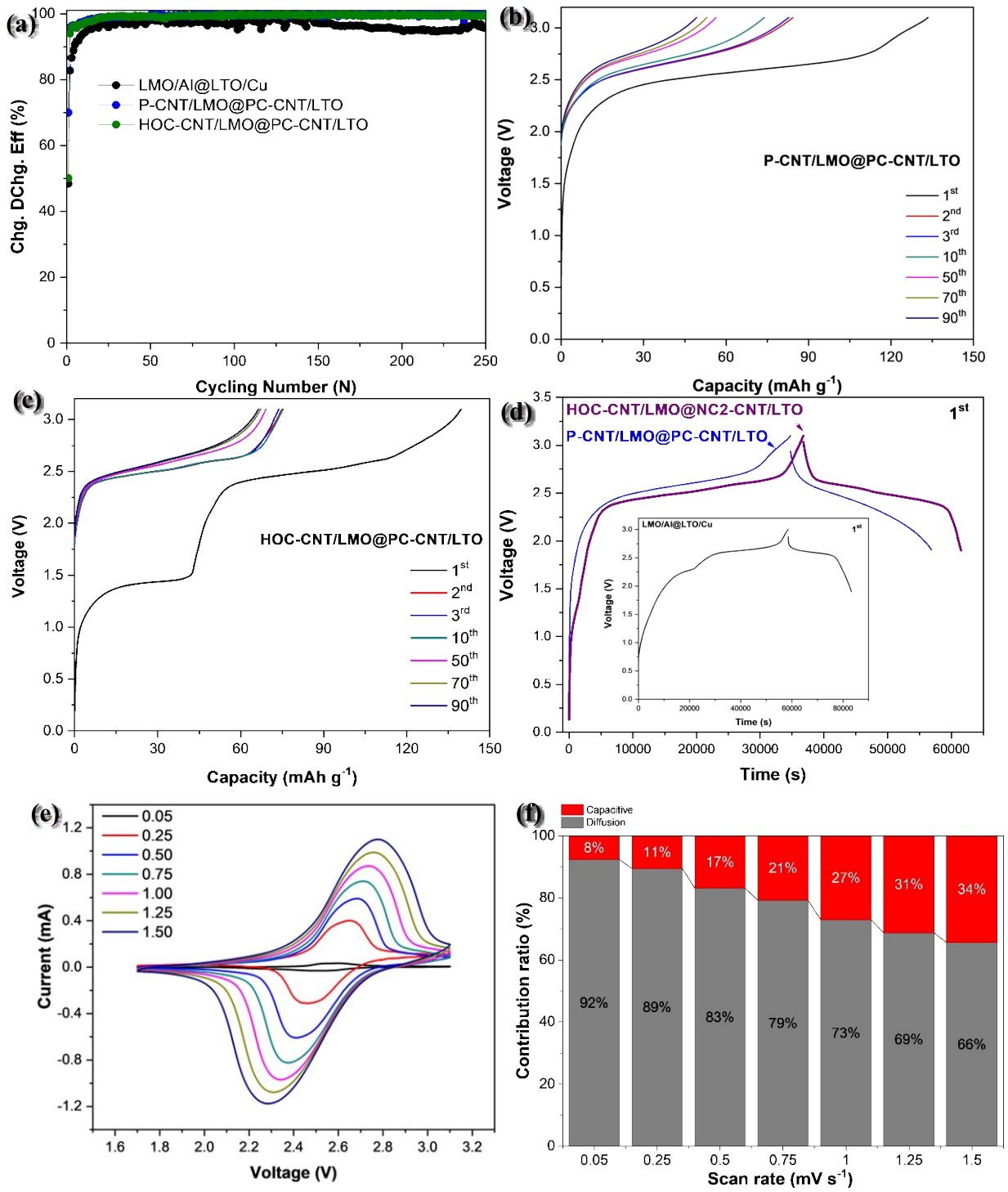
(a)
Chg. DChg. Eff (%)
Cycling Number (N)
LMO/Al@LTO/Cu
P-CNT/LMO@PC-CNT/LTO
HOC-CNT/LMO@PC-CNT/LTO
(b)
Voltage (V)
Capacity (mAh g-1)
P-CNT/LMO@PC-CNT/LTO
1st
2nd
3rd
10th
50th
70th
90th
(c)
Voltage (V)
Capacity (mAh g-1)
HOC-CNT/LMO@PC-CNT/LTO
1st
2nd
3rd
10th
50th
70th
90th
(d)
HOC-CNT/LMO@NC2-CNT/LTO
P-CNT/LMO@PC-CNT/LTO
1st
LMO/Al@LTO/Cu
Voltage (V)
Time (s)
(e)
0.05
0.25
0.50
0.75
1.00
1.25
1.50
Current (mA)
Voltage (V)
(f)
Capacitive
Diffusion
Contribution ratio (%)
8%
11%
17%
21%
27%
31%
34%
92%
89%
83%
79%
73%
69%
66%
Scan rate (mV s-1)

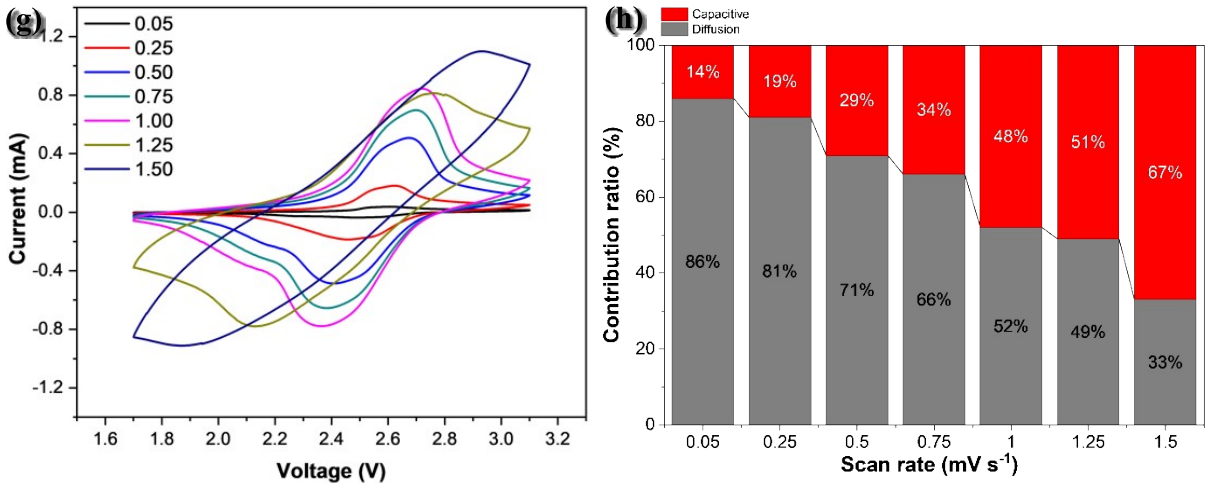


Figure S7. Coulombic Efficiency of (a) LMO/Al@LTO/Cu, P-CNT/LMO@PC-CNT/LTO, and HOC-CNT/LMO@PC-CNT/LTO cells at a cutoff voltage range of 3.1-1.9 V for first cycle and 3.1-1.7 V for subsequent cycles under 0.1C cycling conditions. Charge/discharge voltage profile (b) P-CNT/LMO@PC-CNT/LTO and (c) HOC-CNT/LMO@PC-CNT/LTO. Voltage versus Time (V-t) curves of (d) derived from GCC tests for the three cells LMO/Al@LTO/Cu, P-CNT/LMO@PC-CNT/LTO, and HOC-CNT/LMO@NC2-CNT/LTO. Cyclic voltammetry (CV) curves measured in a two-electrode full-cell configuration (cell voltage referenced to the full-cell potential rather than to a standard reference electrode), together with the quantitative separation of capacitive and diffusion-controlled contributions, for conventional (e-f) LMO/Al@LTO/Cu and (g-h) P-CNT/LMO@NC2-CNT/LTO full cells at different scan rates.

## References

(1) Nyamaa, O.; Nyamaa, U.; Kang, G.-H.; Bayardorj, B.; Yang, J.-H.; Nam, T.-H.; Noh, J.-p. High-Performance Free-Standing LTO/CNT Anodes: Overcoming the Dispersion-Conductivity Trade-Off via Tailored Surface Chemistry for Advanced Full-Cell Architectures. Carbon **2025**, 120391.

(2) Basha, S. S.; Sundari, G. S.; Kumar, K. V.; Reddy, K. V. B.; Rao, M. Electrical conduction behaviour of PVP based composite polymer electrolytes. Rasayan J. Chem **2017**, 10, 279-285.

(3) Bouharras, F. E.; Labardi, M.; Tombari, E.; Capaccioli, S.; Raihane, M.; Améduri, B. Dielectric characterization of core-shell structured poly (vinylidene fluoride)-grafted-BaTiO3 nanocomposites. Polymers **2023**, 15 (3), 595.

(4) Meza-Arroyo, J.; Ramírez-Bon, R. Organic–Inorganic Hybrid Dielectric Layers for Low-Temperature Thin-Film Transistors Applications: Recent Developments and Perspectives. Technologies **2025**, 13 (1), 20.

(5) Salam, M. A.-E.; Elkomy, G.; Osman, H.; Nagy, M.; El-Sayed, F. Structure–electrical conductivity of polyvinylidene fluoride/graphite composites. Journal of Reinforced Plastics and Composites **2012**, 31 (20), 1342-1352.

(6) Nyamaa, O.; Seo, D.-H.; Lee, J.-S.; Jeong, H.-M.; Huh, S.-C.; Yang, J.-H.; Dolgor, E.; Noh, J.-P. High electrochemical performance silicon thin-film free-standing electrodes based on buckypaper for flexible lithium-ion batteries. Materials **2021**, 14 (8), 2053.

(7) Rijal, R.; Lamichhane, H. P.; Pudasainee, K. Molecular structure, homo-lumo analysis and vibrational spectroscopy of the cancer healing pro-drug temozolomide based on dft calculations. AIMS Biophys **2022**, 9 (3), 208-220.